Effect of TiO$_2$ Nanoparticles and Extrusion Process on the Physicochemical Properties of Biodegradable and Active Cassava Starch Nanocomposites

Carolina Iacovone [1], Federico Yulita [1], Daniel Cerini [1], Daniel Peña [1], Roberto Candal [2], Silvia Goyanes [1,3], Lía I. Pietrasanta [3,4], Lucas Guz [2] and Lucía Famá [1,3,*]

1   Laboratorio de Polímeros y Materiales Compuestos (LPMC), Departamento de Física, Facultad de Ciencias Exactas y Naturales, Universidad de Buenos Aires, Buenos Aires C1428EGA, Argentina
2   Instituto de Investigación e Ingeniería Ambiental, Escuela de Hábitat y Sostenibilidad, Campus Miguelete, Universidad Nacional de San Martín, San Martín 1650, Provincia de Buenos Aires, Argentina
3   Instituto de Física de Buenos Aires (IFIBA-CONICET), Facultad de Ciencias Exactas y Naturales, Universidad de Buenos Aires, Buenos Aires C1428EGA, Argentina
4   Centro de Microscopías Avanzadas y Departamento de Física, Facultad de Ciencias Exactas y Naturales, Universidad de Buenos Aires, Buenos Aires C1428EGA, Argentina
*   Correspondence: lfama@df.uba.ar; Tel.: +54-11-5285-7511 (ext. 57511)

Abstract: Biodegradable polymers have been strongly recognized as an alternative to replace traditional petrochemical plastics, which have become a global problem due to their long persistence in the environment. In this work, the effect of the addition of titanium dioxide nanoparticles (TiO$_2$NP) on the morphology, physicochemical properties and biodegradation under industrial composting conditions of cassava starch-based nanocomposites obtained by extrusion at different screw speeds (80 and 120 rpm) were investigated. Films performed at 120 rpm (S$_{120}$ and S$_{120}$-TiO$_2$NP) showed completely processed starch and homogeneously distributed nanoparticles, leading to much more flexible nanocomposites than those obtained at 80 rpm. The incorporation of TiO$_2$NP led to an increase in storage modulus of all films and, in the case of S$_{120}$-TiO$_2$NP, to higher strain at break values. From the Kohlrausch–Williams–Watts theoretical model (KWW), an increase in the relaxation time of the nanocomposites was observed due to a decrease in the number of polymer chains involved in the relaxation process. Additionally, S$_{120}$-TiO$_2$NP showed effective protection against UV light, greater hydrophobicity and faster biodegradation in compost, resulting in a promising material for food packaging applications.

Keywords: starch nanocomposites; TiO$_2$NP; extrusion; tensile strength; UV-shielding; industrial composting

1. Introduction

Plastics are one of the main sources of solid waste in large cities. In particular, the consumption of single-use plastics from food packaging has been identified as a global environmental pollution crisis since they can take up to hundreds of years to decompose [1–3]. Compostable biopolymers offer an efficient solution to plastic pollution since some of them are able to fully biodegrade under adequate environmental conditions [4]. Under composting conditions, polymer biodegradation takes place mainly in two stages. First, fragmentation of polymer chains occurs due to the hydrolysis process initialized by chemical or biological reactions. Then, microorganisms turn the carbon from polymer chains and the oxygen from the air into carbon dioxide (CO$_2$), water and biomass [5]. Biodegradability can be evaluated by quantifying the concentration of CO$_2$ evolved. According to ISO 17088 standards, one of the conditions that plastics must meet to be considered biodegradable under industrial composting conditions is to reach 90% degradation in less than 6 months [6].

The need to reduce the excessive use of single-use plastics that damage the environment generated a great demand for new biodegradable and/or compostable materials with specific properties and easy production. The capabilities of many types of nanocomposites based on biodegradable polymers are currently being explored to try to meet this demand [7–9]. Starch has been one of the most attractive polymers for years to achieve new developments for the packaging industry due to its high capacity to form low-cost and gluten-free biodegradable films [10,11], and because it comes from renewable and highly accessible sources [12,13].

Among processing methods, extrusion is a technique that has been extensively used to produce plastic materials. However, starch extrusion involves multiple chemical and physical reactions, such as gelatinization, decomposition, melting and crystallization [14,15]. Different investigations over the years have shown that the use of glycerol as a plasticizer favors the gelatinization of starch when the water content is limited, as occurs with the extrusion technique [16]. Additionally, shear stress and processing temperature contribute to gelatinization and are relevant parameters to consider in starch extrusion [17]. Recently, Vedove et al. showed the absence of starch granules and broken grains on the surface and fracture surface of cassava starch-glycerol films prepared by extrusion using a screw speed of 80 rpm. González-Seligra et al. showed that the use of 80 rpm and 120 rpm in the extrusion of cassava starch with 20 wt.% of glycerol was very promising to obtain homogeneous thermoplastic starch films [18,19].

The addition of nanofillers, such as silver, zinc oxide and titanium dioxide nanoparticles, has been widely used in science to obtain starch-based nanocomposites for external packaging due to their outstanding properties and antimicrobial characteristics [20–22]. Particularly, titanium dioxide nanoparticles (TiO_2NP) have shown bactericidal capacity against *E. coli* and *S. aureus* and the ability to reflect and absorb UVA (320–400 nm) and UVB (290–320 nm) rays, protecting against sunburn, photoaging and extending product's shelf life after harvesting [23–25]. In addition, FDA has a restriction of titanium dioxide of 1 wt.% when it is used as a food additive [26].

Regarding starch/TiO_2NP, Arezoo et al. and Goudarzi et al. stated that these fillers can efficiently protect products against UV light, being useful as UV-shielding packaging materials [27,28]. Yousef et al. showed that the incorporation of TiO_2NP into thermoplastic starch films prepared by casting led to more flexible materials with higher mechanical resistance while Oleyaei et al. reported a slight increase in the hydrophobicity of potato starch with 1 wt.% of TiO_2NP nanocomposites [29,30].

However, to date, there are few investigations on the effect of TiO_2NP on thermoplastic starch films produced by an industrial technique such as extrusion. Xiong et al. used different concentrations of TiO_2NP in films from potato starch (60%) with glycerol (40%) prepared by blending and obtained nanoparticle agglomeration [31]. However, the authors observed a decrease in the moisture content and an increase in the hydrophobicity, crystallinity and elongation at break of the starch-based nanocomposites due to the incorporation of the nanoparticles. To the best of our knowledge, there are no studies on the compostability under adequate standards of starch materials with TiO_2NP.

This work aims to evaluate the effect of the incorporation of TiO_2NP on the morphology, crystalline structure, mechanical properties, UV-vis absorption and biodegradability under industrial composting conditions of cassava starch-based nanocomposites obtained by extrusion and thermo-compression technology at different processing conditions.

2. Materials and Methods

2.1. Materials

Cassava starch with about 18 wt.% amylose was obtained by C.A.I.S.A. (Costa Rica, Misiones, Argentina), analytical grade glycerol and titanium dioxide nanoparticles (TiO_2NP, mixture of rutile and anatase, purity > 99%) were purchased in Sigma-Aldrich (Merck KGaA, Darmstadt, Germany). TiO_2NP diameter sizes were smaller than 100 nm, according to the manufacturer.

2.2. Films Preparation

Thermoplastic starch films were developed using cassava starch (60%), glycerol (20%) and distilled water (20%) with and without TiO_2NP (1 wt.%) using extrusion at 80 rpm or 120 rpm of screw speed and thermo-compression (defined as S_{80}, S_{80}-TiO_2NP, S_{120} and S_{120}-TiO_2NP). These parameters were chosen from previous studies, in which starch-glycerol films not very sticky and very easy to handle were achieved [32]. A co-rotating twin screw extruder (Nanjing Kerke Extrusion equipment Co., Ltd. Jiangsu, China) was employed with a screw diameter of 16 mm and a length-to-diameter ratio of L/D = 40. The extruder has ten independently controlled temperature zones in the barrel and a 4 mm cylindrical aperture at the end. The temperature profile employed was set at 80 °C/100 °C/110 °C/120 °C/130 °C/140 °C/140 °C/140 °C/130 °C/120 °C for both screw speeds. This temperature profile was chosen considering that in previous works a lower temperature profile was employed at 80 rpm or 120 rpm, which led to some broken starch granules [32,33]. From extrusion process a large thread was obtained that was stabilized in a desiccator at room temperature and relative humidity (RH) of 57% given by a saturated solution of sodium bromide (NaBr). Then, pieces of the thread (~4 g) were used to form films from a thermostatic hydraulic press following Ochoa-Yepes et al. procedure [34]. Samples were placed in between two Teflon sheets in the press and heated at 130 °C for 5 min. Afterward, the pressure was increased up to 1 kPa for 15 min and then to 5 kPa for another 15 min. Finally, the temperature was lowered to 40 °C keeping the pressure at 5 kPa. The resulting films were measured 10 times per system, and all the films resulted of 0.30 ± 0.03 mm in thickness. Films were stored again at 57% RH for 14 days in order to avoid starch retrogradation and evaluate stabilized samples until characterization [35–37].

2.3. Films Characterization

2.3.1. FTIR

ATR-FTIR spectra of all the developed film were recorded in a Jasco FT-IR 4100 spectrometer (Hachioji, Japan) with attenuated total reflectance (ATR) in the range $4000-600 \text{ cm}^{-1}$ with a resolution of 0.4 cm^{-1} and an average of 64 scans. Experiments were carried out in triplicate and no significant differences were observed.

2.3.2. Scanning Electron Microscopy (SEM)

In order to investigate the cross-section morphology of the films, SEM analysis was performed using field emission scanning electron microscopy (FEG-SEM SUPRA40, Overkochen, Alemania). Samples were fractured under liquid nitrogen and then coated with platinum by sputtering before observation.

2.3.3. X-ray Diffraction (XRD)

XRD patterns of starch films were evaluated by a PANalytical Empyrean (Malvern Panalytical, Malvern，UK) using Cu (K-α) radiation (λ =1.54 Å, 40 kV and 30 mA). Samples were scanned over a diffraction angle range of 2θ = 5–35° at a step size of 0.026° and a scan speed of 200 s. A smooth curve connecting the peak baselines was plotted on the diffractograms, and the relative crystallinity was estimated by the ratio of the area above the smooth curve (upper diffraction peak area) over the total diffraction area [38,39].

2.3.4. Water Vapor Permeability (WVP)

Water vapor permeability (WVP) of developed films was determined according to ASTM E-96 procedure with the following modifications [33,40]: Film samples were placed in acrylic permeation cells, with an exposed circular area of $3.8 \times 10^{-4} \text{ m}^2$, previously filled with $CaCl_2$. Cells were conditioned in desiccators at RH of 75% (NaCl) and stored at room temperature to simulate a humidity-controlled chamber. The sealed cell was weighed every

24 h for 7 days. Linear models of the results were performed, and the slope G (g/s) was obtained. Then WVP (g/msPa) was calculated using Equation (1):

$$WVP = \frac{Ge}{A \, DP \, HR} \tag{1}$$

where e (m) is the film thickness, A (m^2) is the test area, DP (Pa) is the saturation vapor pressure of water at room temperature, and HR is the relation of the difference in relative humidity between the cell and the desiccator.

Three replicates were performed for each sample. The mean value and standard deviation are reported.

2.3.5. Moisture Content (MC)

Moisture content (MC) was determined in accordance with the standard method of the AOAC [41]. Samples of each system were initially weighted ($m_i \sim 0.5$ g), dried in an oven at 100 °C for 24 h and then weighted (m_f). Moisture content was calculated as Equation (2):

$$MC = \frac{m_i - m_f}{m_i} \times 100. \tag{2}$$

Assays were carried out in triplicate.

2.3.6. Contact Angle (θ)

The contact angle (θ) was reported as an indicator of the hydrophobicity of the materials. It was determined using an Optical Tensiometer (OneAttension theta—Biolin Scientific, Stockholm, Sweden) at 25 °C, from the angle formed by the tangent of a water drop (2 μL) deposited on the surface of the film and the film surface. Tests were performed in triplicate.

2.3.7. Uniaxial Tensile Properties

Uniaxial tensile properties were studied using Brookfield CT3 Texture Analyzer (Middleborough, MA, USA) at room temperature according to ASTM D882-02 (2002) recommendations at a crosshead speed of 4 mm/min and room temperature [42]. Films with known thickness were cut in strips of 5 mm width and clamped between two jaws with an initial distance of 35 mm Stress-strain curves were recorded and the Young's modulus (E), stress at break (σ_b), strain at break (ε_b) and tensile toughness (T) values were obtained from them. Young's modulus was calculated as the slope of the stress-strain curves in the initial linear region and tensile toughness was determined as the area under the curves up to the point of fracture. At least, 10 replicates were performed for each system.

2.3.8. Mathematical Modeling of KWW

The stress (σ)–strain (ε) curves can be analyzed to consider them as a spectroscopy technique [43] from estimating the average relaxation time <τ> through a known mathematical model, the semi-empirical function Kohlrausch–Williams–Watts (KWW). This model presents the stress σ = σ(ε) for viscoelastic materials as Equation (3):

$$\sigma(\varepsilon) = E_0\varepsilon + E_1(k\tau^*)^{\beta}\left(1 - e^{-\left(\frac{\varepsilon}{k\tau^*}\right)^{\beta}}\right) \tag{3}$$

where k is the strain rate of the test, E_0 is the modulus of the relaxed state (for long times), $E_0 + E_1$ is the initial modulus and $\boldsymbol{\beta}$ is an empirical parameter that takes values between 0 and 1 and quantifies the width of the spectrum of relaxation times. The characteristic time $\boldsymbol{\tau^*}$ is an average relaxation time that characterizes molecular motions in amorphous systems [44], and can be expressed as $\tau^* = <\tau> \times \boldsymbol{\beta}$.

The KWW model on the films was evaluated from the fit of σ-ε curves with Equation (3), from which the parameters $\boldsymbol{\tau^*}$ and $\boldsymbol{\beta}$ were determined.

2.3.9. UV-Vis

UV–vis spectra was studied employing a spectrophotometer (Shimadzu UV-1800, Tokio, Japan). Film samples (1 × 3 cm) were cut and put into a quartz cell, and the absorbance spectrum between 250 and 900 nm was registered. All tests were studied in triplicate presenting no significant differences.

2.3.10. Biodegradability

A Direct Measurement Respirometric (DMR) system based on ISO 14855-1 set up was developed to evaluate the aerobic biodegradation of the films under industrial composting conditions [45]. The DMR system was designed to measure the evolved CO_2 with a CO_2 non-dispersive infrared gas analyzer (NDIR, model MH-Z19 from Zhengzhou Winsen Electronics Technology Co., Zhengzhou, China with a measurement range from 0 to 5000 ppm). DMR was composed of 4 parallel series (Figure 1) in which pressurized air circulates through soda lime to remove the CO_2 present in the air. Then, the air is circulated through a chamber containing deionized water to moisten it, and then through the composting reactor, where the biodegradation process takes place. Afterward, the air is redirected through a water trap (a condenser unit) to remove water vapor from the outflow gas stream before reaching the NDIR sensor. The reactor content (compost and the studied materials) is the only component of the system that is modified between each line. The first line only contains compost (blank), the second a known reference material (native starch powder) and the other two the samples to be measured. In addition, a temperature-controlled system was made by covering the reactors with heating jackets and using a thermosensor to set the temperature at 58 °C, in order to simulate industrial composting conditions.
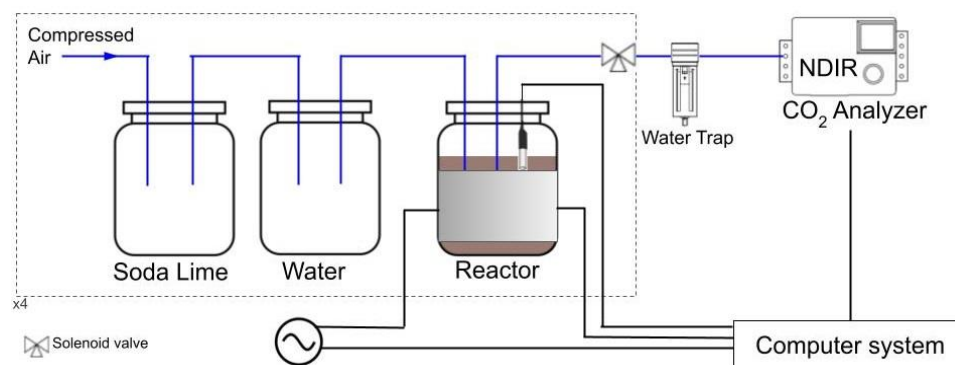
Figure 1. Schematic drawing of direct measurement respirometric system.

The NDIR was used to measure the concentration of CO_2 present in the air outflow from the reactors. Since water condensed after exiting the environmental chamber can damage the NDIR, a water filter (Serie QBM1 G1/4″, Micro Pneumatic S.A.S, Bogotá, Colombia) was installed.

To convert the concentration of CO_2 to mass, Equation (4) was used [46]

$$mCO_2 = \frac{CFT44}{22,414 \times 10^6} \times 100 \tag{4}$$

where mCO_2 is the mass of evolved CO_2 (g), C is the CO_2 concentration (ppm), F is the flow rate, T is the time between each measuring sequence, 22,414 is the volume of 1 mol of gas in cm^3 at STP, 44 is the molecular weight of carbon dioxide (g/mol), and 10^6 is the ppm conversion factor.

The percentage of mineralization (biodegradation) can be determined following Equation (5) and Ref. [45]:

$$\%M = \frac{mCO_2 - mCO_{2b}}{mCO_{2th}} \times 100. \tag{5}$$

where %M is the percentage of mineralization, mCO_2 (g) is the amount of evolved CO_2 in the sample, mCO_{2b} (g) is the amount of evolved CO_2 in the blank, and mCO_{2th} (g) is the theoretical amount of carbon dioxide. The carbon content of the samples was 41%, 42% and 41.2% for starch, S_{120} and S_{120}-TiO_2NP, respectively, determined by Carbon Determination in Soil (SC832 Series Series, LECO, United States of America) and it was used to calculate mCO_{2th}.

For this test, 250 g of industrial compost based on agricultural residues (Orgánicos de Argentina S.A.) with pH 6.8, volatile solids 18 ± 2% and 59 ± 2% humidity was used in each reactor. The compost was sieved on a 2 mm sieve and preconditioned at 58 °C for 3 days before using. Deionized water was incorporated to adjust the moisture content to about 50%. Twenty-five grams of perlite (Terrafertil S.A., Moreno, Argentina) was mixed with the compost and a 3 cm column of perlite was added at the bottom of the reactor to provide better aeration. Twenty grams of samples cut into 2 × 2 cm were mixed with the compost and perlite. On the other hand, native starch powder used as reference was mixed with the compost and perlite. In both cases, a proportion of 1:6 parts (on dry basis) compost was used, as ISO 14855-1:2012 recommends.

During the test, the reactors were incubated in the dark. The compost was stirred and compost humidity was adjusted every day. The CO_2 evolved from the reactors was recorded every 6 h.

To observe the macroscopic physical changes occurring during composting conditions, three films of the 20 g of sample were enclosed in plastic grids and mixed with the rest of the samples, compost and perlite. At 1.5, 3 and 5 days of the test, samples were carefully removed from the grid and photographed. Then, they were taken back into the reactor in order to not interrupt the cumulative CO_2 assessment.

2.3.11. Statistical Analysis

Data analysis was made using Python with $p < 0.05$ de confidence. The reported values are the mean and the error of the mean.

3. Results and Discussion

3.1. FTIR

The main normalized ATR-FTIR spectra of different films are shown in Figure 2. All curves exhibited the typical behavior of thermoplastic starch-based materials [47,48], with a significant absorption peak at $3600-3000 \ cm^{-1}$ attributed to the O–H stretching vibration due to free and inter- and intra-molecular hydrogen bonding of the films [49]; a double peak at 2930 and 2850 cm^{-1} associated the symmetric and asymmetric C-H stretching; and a peak at 1640 cm^{-1} assigned to the water adsorbed by starch molecules, among others. There are no changes in the wave number of the bands nor the appearance of new bands due to the different processing or the nanoparticle's addition. However, after the incorporation of TiO_2NP, slight broadening in the 3300 cm^{-1} band was observed. This behavior suggests an increased degree of hydrogen bonding since oxygen atoms in TiO_2 formed hydrogen bonding with H atoms of the OH groups in the starch [30,50].

3.2. Morphology

FE-SEM micrographs of the cryogenic fracture surface of the films showed some broken starch grains in the matrix made at 80 rpm (Figure 3a, marked with arrows, and Figure 3e), which seem to have fully processed with the use of 120 rpm (S_{120}). This suggests that the higher mechanical energy produced by the increase in the screw speed contributed to the improvement in the complete process of the starch grains.
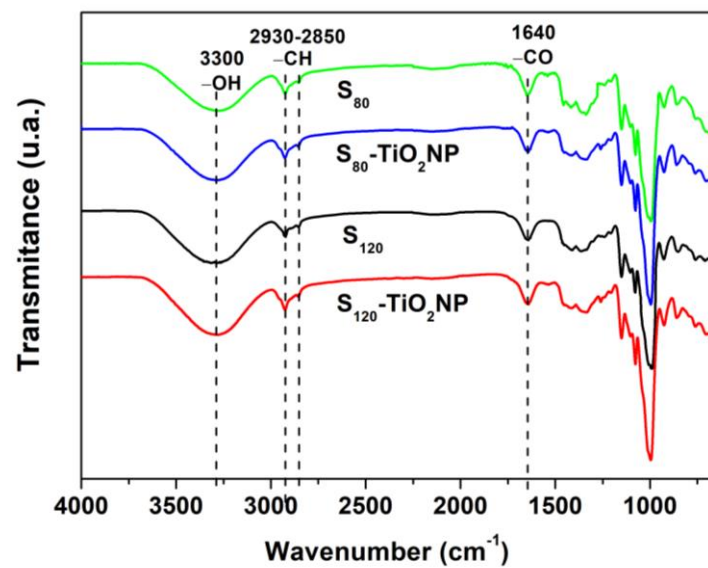
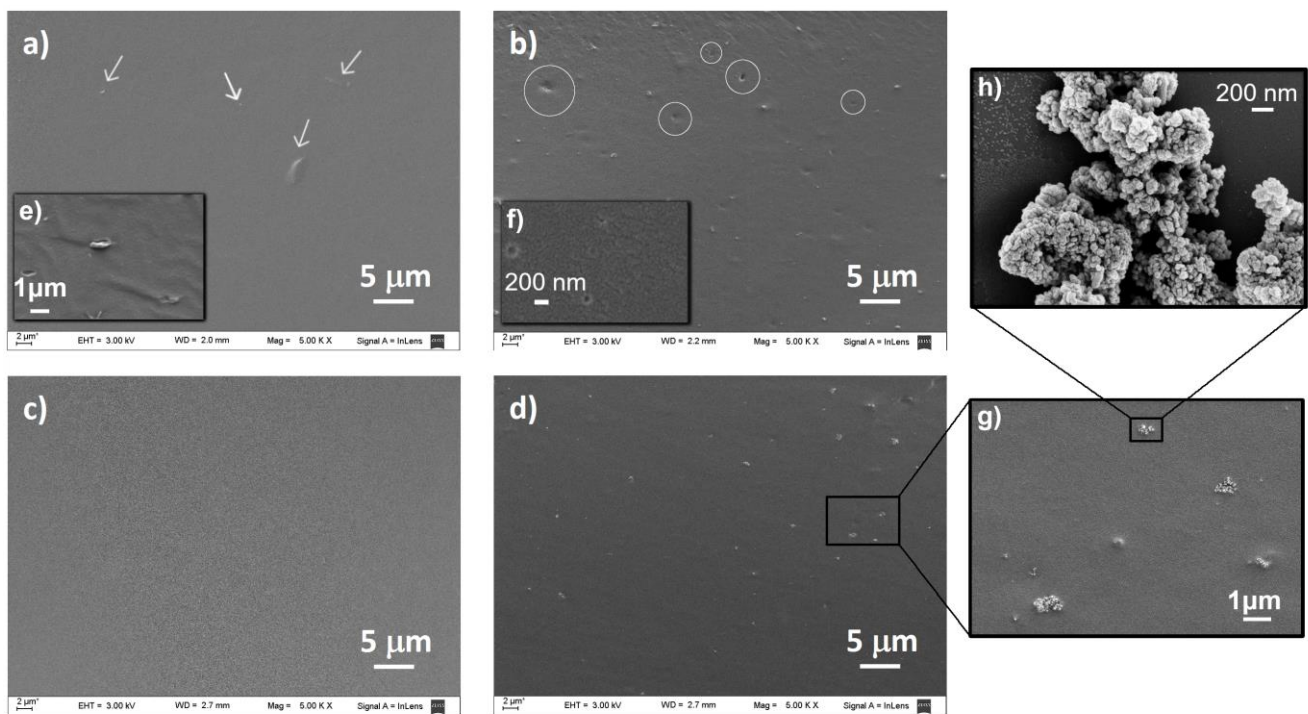**Figure 2.** FTIR spectrum of the different studied films.

Figure 3. SEM micrographs of the cryogenic fracture surface of (**a**) S_{80}, (**b**) S_{80}-TiO$_2$NP, (**c**) S_{120} and (**d**) S_{120}-TiO$_2$NP. Arrows indicate broken starch grains, which can be seen with higher magnification in (**e**), and circles indicate holes that can be seen with higher magnification in (**f**–**h**) show higher magnification of nanoparticle agglomeration.

The incorporation of TiO$_2$NP behaved markedly differently depending on the nanocomposite manufacturing process. While in the case of S_{80}-TiO$_2$NP an inhomogeneous distribution of nanoparticles was observed with the presence of some holes, in the nanocomposite prepared at 120 rpm a great improvement in the distribution of the nanofiller and prevention of holes generation was found (Figure 3b,d). In an image of S_{120}-TiO$_2$NP with higher magnification (Figure 3g,h), it can be seen nanoparticles agglomerations. Nevertheless, the agglomerates seem to be homogeneously dispersed (Figure 3b,g).

3.3. X-ray Diffraction

Figure 4 presents the X-ray diffraction patterns of the different samples. Diffraction peaks centered at 11.7°, 14.8°, 16.9° and 18° are related to A-type structure and those at 22.2° and 24.2° correspond to B-type structure [51]. These peaks are related to the retrogradation of starch during storage, although there could be a contribution from some non-gelatinized granules [19,51,52]. Peaks at 12.9° and 19.6° correspond to V_h-type structure, related to the insertion of glycerol molecules within the starch helical structure [51].
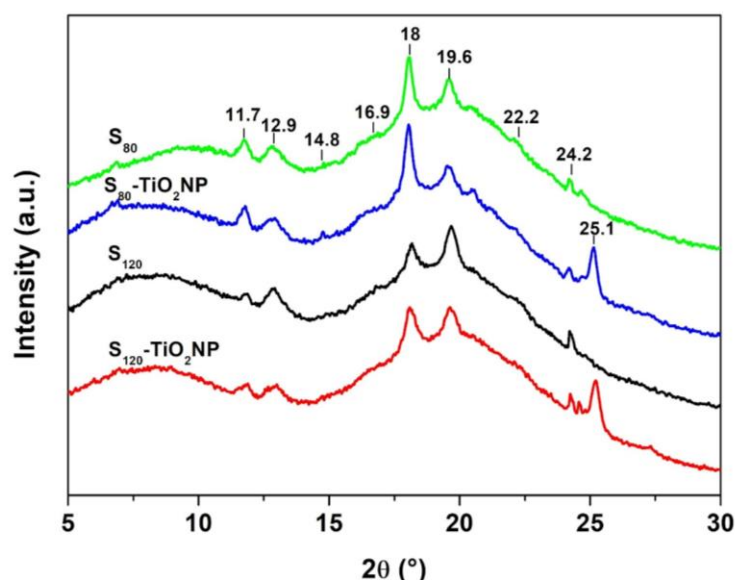
Figure 4. X-ray diffraction patterns of S_{80}, S_{80}-TiO$_2$NP, S_{120}, and S_{120}-TiO$_2$NP.

Relevant changes in X-ray pattern and relative crystallinity (RC) of the films were observed when starch was processed at different rpm. The relative intensity of the peak at 18° decreased while that of the peaks corresponding to the Vh-type structure at 19.6° increased in S_{120} samples compared to S_{80} (Figure 4). These results are due to a better starch processing in S_{120} and thus to the possible greater interaction between starch and glycerol, suggesting that more glycerol molecules are within the helical structure of the starch in this film [33,53]. As a consequence, lower RC values were obtained for the films processed at 120 rpm (Table 1).

Table 1. Relative crystallinity of the films obtained from the X-ray diffraction patterns.

Peaks (°)	Type	Relative Crystallinity (%) [±0.2]			
		S_{80}	S_{80}-TiO$_2$NP	S_{120}	S_{120}-TiO$_2$NP
18	A	2.7	3.7	1.7 [a]	2.0 [a]
19.6	V_h	2.0 [a]	1.9 [a]	2.7	2.0 [a]
25.1	Titanium	0	3.3 [a]	0	3.4 [a]
Total	A-B-V_h	8.2	12.5	7.4	10.5

[a] Values with the same letters in the files are not significantly different ($p > 0.05$).

With TiO$_2$NP incorporation, the characteristic peak of V_h-type crystalline structure at 19.6° decrease in S_{120}-TiO$_2$NP, which demonstrates that the nanoparticles could have restricted the recrystallization of molecular starch, as has already been reported in the literature [31], since they may act as nucleation centers in a starch matrix [54]. Furthermore, a new peak at around 25.2° appears in the films containing the nanofillers, which is characteristic of TiO$_2$ nanoparticles [31], and causes an increase in the relative crystallinity of the nanocomposites.

3.4. Water Vapor Permeability (WVP)

WVP values did not show significant differences between the films, as can be shown in Table 2. A trend towards an increase in WVP of S_{80} compared to S_{120} is observed, which could be due to the more tortuous path for water due to the presence of broken starch grains. The incorporation of TiO_2NP decreases WVP of S_{80}-TiO_2NP and increases it in S_{120}-TiO_2NP. In the first case, the behavior could be associated with the presence of some holes in S_{80}-TiO_2NP that favored the diffusion of water molecules through the film, leading to increases in WVP. In the case of S_{120}-TiO_2NP, it would be due to the greater distribution of TiO_2NP in this nanocomposite with respect to S_{80}-TiO_2NP. The presence of well-dispersed nanoparticles could increase the tortuous path by dispersing water molecules and thus decreasing the diffusion rate.

Table 2. Results of water vapor permeability (WVP), moisture content (MC) and contact angle (θ) of the developed materials.

	WVP	**MC (%) [± 1]**	**θ (°)**
S_{80}	1.1 ± 0.1 [a]	18 [a]	70 ± 3 [a]
S_{120}	1.3 ± 0.3 [a]	22	70 ± 3 [a]
S_{80}-TiO_2NP	1.4 ± 0.4 [a]	18 [a]	64 ± 4 [a]
S_{120}-TiO_2NP	0.9 ± 0.1 [a]	19 [a]	77 ± 3

[a] Values with the same letters in the columns are not significantly different ($p > 0.05$).

3.5. Moisture Content (MC)

Table 2 shows a slight decrease in the moisture content (MC) of S_{80} compared to S_{120} perhaps as a result of its higher crystallinity since, as it is known an increase in crystallinity leads to a decrease in MC [55,56]. The addition of the nanoparticles led to a slight decrease in MC in the case of S_{120}-TiO_2NP and was explained by the stable hydrogen bonds between TiO_2NP and matrix components leading to a decrease in the number of water molecules with the possibility of being captured by starch. Thereby, the penetration of water molecules is more difficult, increasing the water resistance of the nanocomposites, as shown in the literature on starch-TiO_2NP nanocomposites prepared by casting [28,30].

3.6. Contact Angle (θ)

As can be seen in Table 2, no significant differences in contact angle values were observed between S_{80} and S_{120}, nor with the addition of TiO_2NP. A decreasing trend of θ in S_{80}-TiO_2NP can be observed compared to S_{80} (Figure 5), possibly due to the presence of some holes in this nanocomposite, which leads to an increase in the water drop absorption and thus in the hydrophilicity of the film. In contrast, in the case of S_{120}-TiO_2NP, a more hydrophobic film was obtained. This was possible as a consequence of the strong hydrogen bonding interaction between the nanoparticles and the matrix that left fewer OH groups available to interact with the water drop, as seen in MC and ATR-FTIR measurements [31].

3.7. Uniaxial Tensile Properties

Figure 6 shows the tensile stress (σ)–strain (ε) curves of all films, which exhibit the typical behavior for thermoplastic starch materials [57]: a linear elastic zone followed by a non-linear elastic zone until failure. The stress at break (σ_b), strain at break (ε_b), Young's modulus (E) and toughness (T) values obtained from the σ-ε curves, as well as the parameters from the theoretical KWW model are shown in Table 3. Relevant differences were observed between the films produced at different rpm. S_{80} presented higher E and σ_b values but lower strain at break than S_{120} and no significant differences in T. The increase in E was expected due to the presence of starch granules in S_{80}, as shown in SEM images (Figure 3a), which led to a more crystalline material (as seen in XRD). The broken grains may have been the cause of early material failure due to faster crack propagation produced during the deformation.
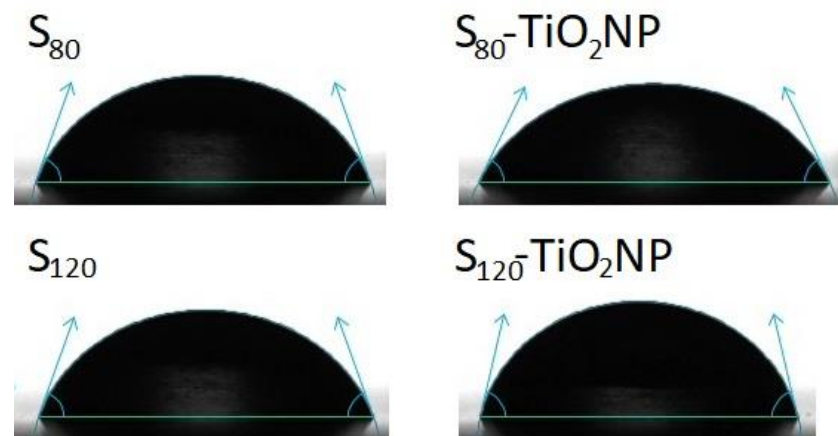
Figure 5. Image of the drop of distilled water deposited on the surface of the films.
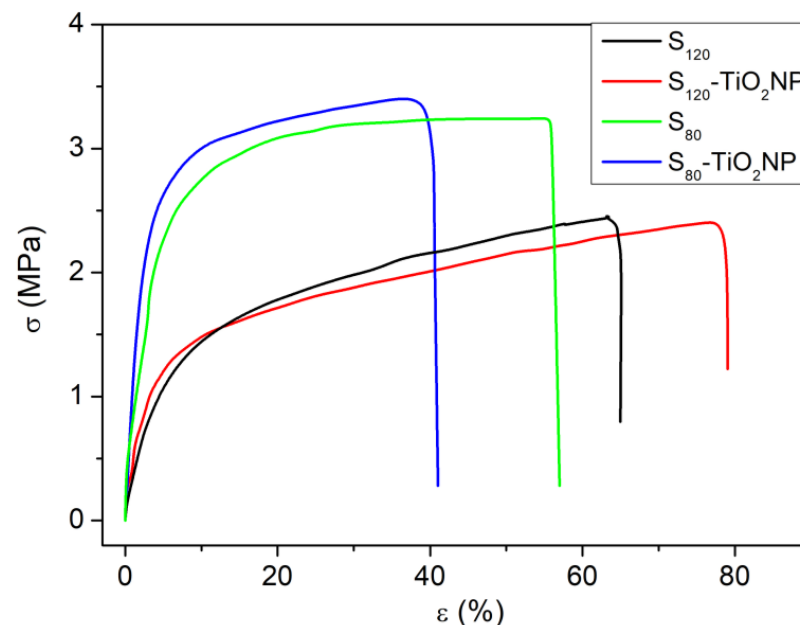

Figure 6. Tensile stress (σ)–strain (ε) curves of S_{80}, S_{80}-TiO$_2$NP, S_{120} and S_{120}-TiO$_2$NP.

Table 3. Results of the Young's modulus (E), stress at break (σ_b), strain at break (ε_b), tensile toughness (T), and the parameters from the theoretical Kohlrausch–Williams–Watts (KWW) model (τ^* and β).

	E (MPa)	σ_b (MPa)	ε_b (%) [±4]	*T* (MJ/m^3)	τ^*	β
S_{80}	81.5 ± 0.8	3.2 ± 0.3 [a]	57	1.6 ± 0.2 [a]	26.28 ± 0.03	0.820 ± 0.001
S_{120}	39.6 ± 0.7	2.7 ± 0.2 [a,b]	66	1.3 ± 0.1 [a,b]	178 ± 2	0.511 ± 0.003
S_{80}-TiO$_2$NP	87.3 ± 0.8	3.4 ± 0.3 [a]	41	1.2 ± 0.1 [b]	28.63 ± 0.07	1.000 ± 0.003
S_{120}-TiO$_2$NP	48.5 ± 0.6	2.5 ± 0.3 [b]	79	1.5 ± 0.5 [a,b]	32.08 ± 0.3	0.634 ± 0.001

[a,b] Values with the same letters are not significantly different ($p > 0.05$).

The addition of TiO$_2$NP showed different effects depending on the type of processing performed. In both cases, increases in E were obtained due to the higher modulus of TiO$_2$NP compared to the starch matrix, being around 20% in S_{120}-TiO$_2$NP. The strain at break markedly decreased in S_{80}-TiO$_2$NP and increased in the nanocomposite prepared at 120 rpm probably due to the well-dispersed nanoparticles in S_{120}-TiO$_2$NP. It is not so common to find in the literature nanocomposites with increases in ε_b, since nanoparticles incorporation frequently generates early propagation of failures [30,58]. Increases in the strain at break were reported in starch-TiO$_2$NP bionanocomposite prepared by blending [35] and in chitosan/starch blend-based films with 1 wt.% of TiO$_2$NP [31,59]. These last

authors showed that when NP presented heterogeneous dispersion in the polymeric matrix, decreases in εb occurred, concluding that heterogeneity could act as stress concentrator.

Regarding KKW model, an increase in τ^* and a decrease in β with increasing extrusion speed. This was expected considering that when 120 rpm is used, the crystalline phase decreases due to the better processing of the starch grains, as previously discussed. With the addition of nanoparticles, a marked decrease in τ^* and a slight increase in β was obtained in the case of S_{120}-TiO, suggesting that the nanoparticles tend to increase the number of polymeric molecules involved in the relaxation process, which was related to the highest elongation of this nanocomposite.

3.8. UV-Vis

Figure 7 shows the UV-vis absorbance spectra of the samples, where S_{80} was similar to S_{120}. As can be observed, there was a drastic difference in the curves between the matrix and the nanocomposites. S_{120}-TiO$_2$NP and S_{80}-TiO$_2$NP presented an absorption peak at around 340 nm, which is not observed in the matrices. This phenomenon is explained by considering that TiO$_2$NP has UV shielding properties and, consequently, the starch-nanocomposites containing this nanofiller should present good UV shielding ability [60]. UV shielding properties were observed in starch films containing 1 wt.% of TiO$_2$NP prepared by casting [28,30]. S_{120}-TiO$_2$NP and S_{80}-TiO$_2$NP did not present significant differences, indicating that the screw speed during the material's process does not change light absorption properties.
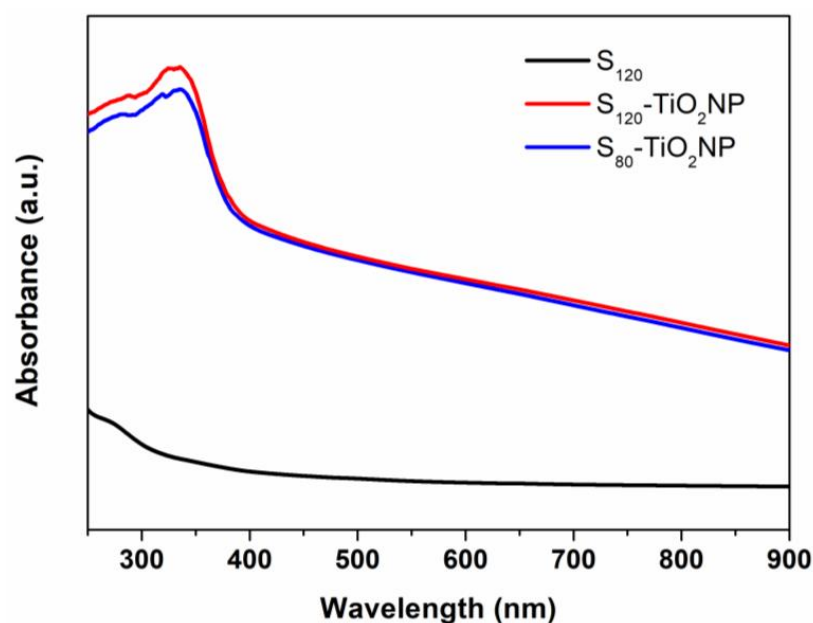

Figure 7. UV–vis absorption spectra of Starch and Starch/TiO$_2$ nanocomposite films.

3.9. Biodegradability

Based on the improved properties of the materials produced at 120 rpm over those prepared at 80 rpm, biodegradability tests were performed on S_{120} and S_{120}-TiO$_2$NP. The percentage mineralization curves obtained from cumulative CO$_2$ evolution as a function of composting time are presented in Figure 8.

During the first 10 days, the mineralization rate of starch (reference) was higher than that of S_{120}, and afterward, both materials' biodegradation rates were similar almost all of the time. S_{120} mineralization's curve is similar, as shown in the literature in starch-based films prepared by extrusion, and its initial slower biodegradation could be a consequence of the lower surface area of the films compared to starch powder [61,62]. Briassoulis et al. observed similar behavior when comparing the biodegradation in soils of PHB [63]. In powder PHB, the authors observed a higher initial biodegradation rate than in 2 × 2 cm

films. The fast mineralization curve of starch powder is possible because it has a higher surface area than films and it is easily available for microbial assimilation [64].
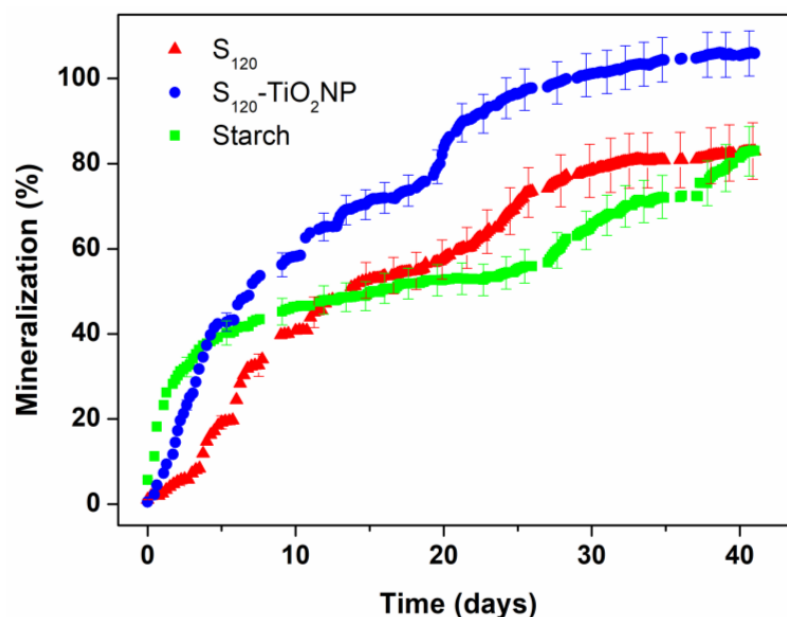

Figure 8. Percentage mineralization as a function of time for S_{120}, S_{120}-TiO$_2$NP and starch in the DMR system. Mineralization error bars for the replicates are represented at selective times to facilitate the reading of the plots.

The incorporation of TiO$_2$ nanoparticles noticeably accelerated the biodegradation rate and increased the final biodegradation percentage of S_{120}-TiO$_2$NP compared to S_{120} and the reference. This behavior has not been previously observed in starch nanocomposites. Luo et al., obtained higher biodegradation rates under industrial composting conditions of (Poly-lactic) acid films when incorporating TiO$_2$NP [65], suggesting that this behavior could be related to hydrolytic degradation, since TiO$_2$NP may accelerate some hydrolytic reactions. Similarly, Del Campo et al. observed that the incorporation of ZnO in a biodegradable commercial polymer (Ecovio) significantly accelerates the disintegration process under a composting environment [66–68], indicating that the nanoparticles could initiate or advance some hydrolytic reactions. It was expected that the incorporation of TiO$_2$NP delayed the starch film biodegradation since it is well-known that these nanoparticles provide antimicrobial activity to polymeric nanocomposites [69,70]. However, in this work, antimicrobial activity was evaluated by the halo inhibition assay in agar plates and no activity was observed (see Supplementary Materials). Water and microorganisms could damage the interface between the starch matrix and nanoparticles, increasing the possibility of hydrolysis, as Zamir et al. proposed from the higher degradation rate of PLA films when starch nanoparticles were incorporated [71].

At the end of the test, after 42 days, S_{120}-TiO$_2$NP, S_{120}, and powder starch reached $106 \pm 5\%$, $83 \pm 7\%$ and $83 \pm 6\%$ biodegradation, respectively. S_{120}-TiO$_2$NP showed greater mineralization than 100%, which according to the literature is an indication of the priming effect attributed to the over-degradation of the indigenous organic carbon present in the compost when glucose and its polymers are tested [64,72–74]. According to ISO 14855-1 and the European Standard EN 13432, S_{120}-TiO$_2$NP can be identified as biodegradable since its percentage of mineralization was greater than 90% and that of the positive control (powder cassava starch) was greater than 70% [45,75].

Figure 9 shows the macroscopic appearance of the films at different times of disintegration in the DMR system. After only 1.5 days of testing, fragmentation was observed in both samples due to the absorption of water and the adhesion of organic matter on them. The films already started to break down in pieces mainly due to the fast hydrolytic

degradation process. This behavior was more noticeable in S_{120}-TiO_2NP, where more pieces were disintegrated compared to S_{120}. On the 3rd day, only a very few pieces of S_{120}-TiO_2NP were observed, while on the 5th day a total degradation was noticed and S_{120} still presented many pieces.
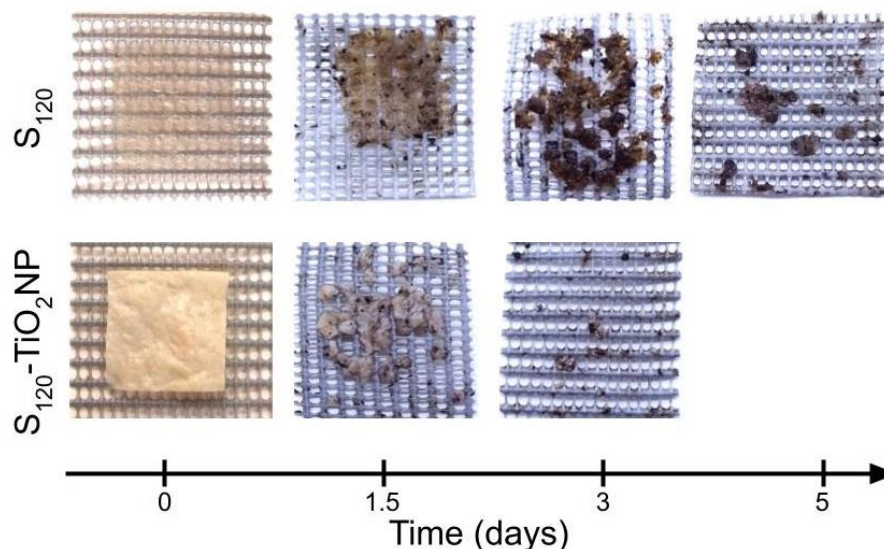
Figure 9. Photographs of the tested materials at different timings of the degradation process.

Even though the films had almost completely disappeared by the third day and fifth day, their biodegradation process had not been completed, as can be seen in Figure 8. This occurs because in the initial degradation steps the material fragments and forms microplastics that still contain organic carbon that could undergo microbial biodegradation and be converted into CO_2. These results demonstrate the relevance of determining materials biodegradability by employing respirometric assays, since macroscopic analysis could underestimate the required time for the complete mineralization, especially in the case of fast-degrading polymers such as starch-based films.

The results of biodegradation tests show that TiO_2NP significantly accelerates the disintegration process of starch-based nanocomposites under an industrial composting environment.

4. Conclusions

The investigation of biodegradable polymers as an alternative to replace traditional petrochemical plastics for environmental preservation is relevant nowadays. In the present study, the extrusion processing conditions of cassava starch films and the incorporation of TiO_2NP in thermoplastic starch-based nanocomposites were evaluated. Increasing the extrusion screw speed from 80 rpm to 120 rpm led to materials with lower crystallinity that can withstand greater deformations before breaking and nanocomposites with TiO_2NP homogeneously dispersed in the starch matrix. Based on the results, greater hydrophobicity in the nanocomposites prepared at 120 rpm was observed due to the destruction of the hydrogen bond formed between the O in H_2O and the H in C-O-H of the starch by the addition of TiO_2NP, which also led to higher Young's modulus and relaxation time values. The characteristics of TiO_2NP were reflected in the effectiveness of the UV light protection of the films for their possible use in light-blocking packaging and in their greater crystallinity. This investigation revealed that TiO_2NP used in starch films initiated or advanced some hydrolytic reactions under industrial composting conditions, accelerating the disintegration and biodegradation of the material. It was concluded that the use of TiO_2NP in cassava starch-based materials could be promising for its use as fast degrading material under industrial composting conditions and light-blocking packaging with improved mechanical resistance.

References

1. UN Environment Programme Single-Use Plastics: A Roadmap for Sustainability. Available online: http://www.unep.org/resources/report/single-use-plastics-roadmap-sustainability (accessed on 5 January 2023).
2. Chamas, A.; Moon, H.; Zheng, J.; Qiu, Y.; Tabassum, T.; Jang, J.H.; Abu-Omar, M.; Scott, S.L.; Suh, S. Degradation rates of plastics in the environment. *ACS Sustain. Chem. Eng.* **2020**, *8*, 3494–3511. [CrossRef]
3. Chen, Y.; Awasthi, A.K.; Wei, F.; Tan, Q.; Li, J. Single-use plastics: Production, usage, disposal, and adverse impacts. *Sci. Total Environ.* **2021**, *752*, 141772. [CrossRef] [PubMed]
4. Notaro, S.; Lovera, E.; Paletto, A. Consumers' Preferences for Bioplastic Products: A Discrete Choice Experiment with a Focus on Purchase Drivers. *J. Clean. Prod.* **2022**, *330*, 129870. [CrossRef]
5. Castro Aguirre, E. Design and Construction of A Medium-Scale Automated Direct Measurement Respirometric System to Assess Aerobic Biodegradation of Polymers. Master's Thesis, Michigan State University, East Lansing, MI, USA, 2013.
6. *ISO 17088*; Plastics—Organic Recycling—Specifications for Compostable Plastics. ISO: Geneva, Switzerland, 2021.
7. García, N.; Famá, L.; D'accorso, N.; Goyanes, S. Biodegradable Starch Nanocomposites. In *Eco-Friendly Polymer Nanocomposites*; Springer: New Delhi, India, 2015; Volume 75, pp. 17–77.
8. Omerović, N.; Djisalov, M.; Živojević, K.; Mladenović, M.; Vunduk, J.; Milenković, I.; Knežević, N.Ž.; Gadjanski, I.; Vidić, J. Antimicrobial nanoparticles and biodegradable polymer composites for active food packaging applications. *Compr. Rev. Food Sci. Food Saf.* **2021**, *20*, 2428–2454. [CrossRef] [PubMed]
9. Glaskova-Kuzmina, T.; Starkova, O.; Gaidukovs, S.; Platnieks, O.; Gaidukova, G. Durability of biodegradable polymer nanocomposites. *Polymers* **2021**, *13*, 3375. [CrossRef]
10. Onyeaka, H.; Obileke, K.; Makaka, G.; Nwokolo, N. Current research and applications of starch-based biodegradable films for food packaging. *Polymers* **2022**, *14*, 1126. [CrossRef]
11. Horstmann, S.W.; Lynch, K.M.; Arendt, E.K. Starch characteristics linked to gluten-free products. *Foods* **2017**, *6*, 29. [CrossRef]
12. Ponnusamy, P.G.; Mani, S. Material and environmental properties of natural polymers and their composites for packaging applications—A review. *Polymers* **2022**, *14*, 4033. [CrossRef]
13. García-Guzmán, L.; Cabrera-Barjas, G.; Soria-Hernández, C.G.; Castaño, J.; Guadarrama-Lezama, A.Y.; Rodríguez Llamazares, S. Progress in Starch-based materials for food packaging applications. *Polysaccharides* **2022**, *3*, 136–177. [CrossRef]
14. Liu, H.; Xie, F.; Yu, L.; Chen, L.; Li, L. Thermal processing of starch-based polymers. *Prog. Polym. Sci.* **2009**, *34*, 1348–1368. [CrossRef]
15. López, O.V.; García, M.A. Starch Films from a Novel (Pachyrhizus Ahipa) and conventional sources: Development and characterization. *Mater. Sci. Eng. C* **2012**, *32*, 1931–1940. [CrossRef] [PubMed]
16. Tan, I.; Wee, C.C.; Sopade, P.A.; Halley, P.J. Estimating the specific heat capacity of starch-water-glycerol systems as a function of temperature and compositions. *Starch-Stärke* **2004**, *56*, 6–12. [CrossRef]
17. Jbilou, F.; Ayadi, F.; Galland, S.; Joly, C.; Dole, P.; Belard, L.; Degraeve, P. Effect of Shear Stress Extrusion Intensity on Plasticized Corn Flour Structure: Proteins Role and Distribution. *J. Appl. Polym. Sci.* **2012**, *123*, 2177–2186. [CrossRef]
18. Vedove, T.M.; Maniglia, B.C.; Tadini, C.C. Production of sustainable smart packaging based on cassava starch and anthocyanin by an extrusion process. *J. Food Eng.* **2021**, *289*, 110274. [CrossRef]

19. González-Seligra, P.; Guz, L.; Ochoa-Yepes, O.; Goyanes, S.; Famá, L. Influence of extrusion process conditions on starch film morphology. *LWT* **2017**, *84*, 520–528. [CrossRef]

20. Ceballos, R.L.; von Bilderling, C.; Guz, L.; Bernal, C.; Famá, L. Effect of greenly synthetized silver nanoparticles on the properties of active starch films obtained by extrusion and compression molding. *Carbohydr. Polym.* **2021**, *261*, 117871. [CrossRef]

21. Priyadarshi, R.; Roy, S.; Ghosh, T.; Biswas, D.; Rhim, J.-W. Antimicrobial nanofillers reinforced biopolymer composite films for active food packaging applications—A review. *Sustain. Mater. Technol.* **2021**, *32*, e00353. [CrossRef]

22. Abdollahzadeh, E.; Nematollahi, A.; Hosseini, H. Composition of antimicrobial edible films and methods for assessing their antimicrobial activity: A review. *Trends Food Sci. Technol.* **2021**, *110*, 291–303. [CrossRef]

23. Yong, S.-S.; Lee, J.-I.; Kang, D.-H. TiO$_2$-Based photocatalyst generated reactive oxygen species cause cell membrane disruption of *Staphylococcus aureus* and *Escherichia Coli* O157: H7. *Food Microbiol.* **2023**, *109*, 104119. [CrossRef]

24. Sanches, P.L.; Geaquinto LR, D.O.; Cruz, R.; Schuck, D.C.; Lorencini, M.; Granjeiro, J.M.; Ribeiro AR, L. Toxicity evaluation of TiO$_2$ nanoparticles on the 3D skin model: A systematic review. *Front. Bioeng. Biotechnol.* **2020**, *8*, 575. [CrossRef]

25. Zhang, W.; Rhim, J.-W. Titanium Dioxide (TiO$_2$) for the Manufacture of Multifunctional Active Food Packaging Films. *Food Packag. Shelf Life* **2022**, *31*, 100806. [CrossRef]

26. FDA Summary of Color Additives for Use in the United States in Foods, Drugs, Cosmetics, and Medical Devices. Available online: https://www.fda.gov/industry/color-additive-inventories/summary-color-additives-use-united-states-foods-drugs-cosmetics-and-medical-devices#ftnote7 (accessed on 5 January 2023).

27. Arezoo, E.; Mohammadreza, E.; Maryam, M.; Abdorreza, M.N. The synergistic effects of cinnamon *Essential Oil* and Nano TiO$_2$ on antimicrobial and functional properties of sago starch films. *Int. J. Biol. Macromol.* **2020**, *157*, 743–751. [CrossRef] [PubMed]

28. Goudarzi, V.; Shahabi-Ghahfarrokhi, I.; Babaei-Ghazvini, A. Preparation of ecofriendly UV-Protective food packaging material by Starch/TiO$_2$ Bio-nanocomposite: Characterization. *Int. J. Biol. Macromol.* **2017**, *95*, 306–313. [CrossRef]

29. Yousefi, A.R.; Savadkoohi, B.; Zahedi, Y.; Hatami, M.; Ako, K. Fabrication and characterization of hybrid sodium montmorillonite/TiO$_2$ reinforced cross-linked wheat starch-based nanocomposites. *Int. J. Biol. Macromol.* **2019**, *131*, 253–263. [CrossRef] [PubMed]

30. Oleyaei, S.A.; Zahedi, Y.; Ghanbarzadeh, B.; Moayedi, A.A. Modification of physicochemical and thermal properties of starch films by incorporation of TiO$_2$ nanoparticles. *Int. J. Biol. Macromol.* **2016**, *89*, 256–264. [CrossRef]

31. Xiong, J.; Sheng, C.; Wang, Q.; Guo, W. Toughened and water-resistant starch/TiO$_2$ Bio-nanocomposites as an environment-friendly food packaging material. *Mater. Res. Express* **2019**, *6*, 055045. [CrossRef]

32. Ceballos, R.L.; Ochoa-Yepes, O.; Goyanes, S.; Bernal, C.; Famá, L. Effect of yerba mate extract on the performance of starch films obtained by extrusion and compression molding as active and smart packaging. *Carbohydr. Polym.* **2020**, *244*, 116495. [CrossRef]

33. Guz, L.; González-Seligra, P.; Ochoa-Yepes, O.; Estevez-Areco, S.; Famá, L.; Goyanes, S. Influence of different commercial modified cassava starches on the physicochemical properties of thermoplastic edible films obtained by flat-die extrusion. *Starch-Stärke* **2021**, *73*, 2000167. [CrossRef]

34. Ochoa-Yepes, O.; Medina-Jaramillo, C.; Guz, L.; Famá, L. Biodegradable and edible starch composites with fiber-rich lentil flour to use as food packaging. *Starch-Stärke* **2018**, *70*, 1700222. [CrossRef]

35. Famá, L.; Goyanes, S.; Gerschenson, L. Influence of storage time at room temperature on the physicochemical properties of cassava starch films. *Carbohydr. Polym.* **2007**, *70*, 265–273. [CrossRef]

36. Mali, S.; Grossmann, M.V.E.; García, M.A.; Martino, M.N.; Zaritzky, N.E. Effects of controlled storage on thermal, mechanical and barrier properties of plasticized films from different starch sources. *J. Food Eng.* **2006**, *75*, 453–460. [CrossRef]

37. Schmitt, H.; Guidez, A.; Prashantha, K.; Soulestin, J.; Lacrampe, M.; Krawczak, P. Studies on the effect of storage time and plasticizers on the structural variations in thermoplastic starch. *Carbohydr. Polym.* **2015**, *115*, 364–372. [CrossRef] [PubMed]

38. Cheetham, N.W.; Tao, L. Variation in crystalline type with amylose content in maize starch granules: An X-Ray powder diffraction study. *Carbohydr. Polym.* **1998**, *36*, 277–284. [CrossRef]

39. Grande, C.J.; Torres, F.G.; Gomez, C.M.; Troncoso, O.P.; Canet-Ferrer, J.; Martínez-Pastor, J. Development of self-assembled bacterial cellulose–starch nanocomposites. *Mater. Sci. Eng. C* **2009**, *29*, 1098–1104. [CrossRef]

40. *ASTM E-96*; Standard Test Methods for Water Vapor Transmission of Materials. ASTM International: West Conshohocken, PA, USA, 2016.

41. AOAC. *Official Methods of Analysis*; Association of official analytical chemists: Washington, DC, USA, 1995.

42. *ASTM D882-02*; Standard Test Method for Tensile Properties of Thin Plastic Sheeting. ASTM International: West Conshohocken, PA, USA, 2002.

43. Mano, J.F.; Viana, J. Effects of the strain rate and temperature in stress–strain tests: Study of the glass transition of a polyamide-6. *Polym. Test.* **2001**, *20*, 937–943. [CrossRef]

44. Shamblin, S.L.; Hancock, B.C.; Dupuis, Y.; Pikal, M.J. Interpretation of relaxation time constants for amorphous pharmaceutical systems. *J. Pharm. Sci.* **2000**, *89*, 417–427. [CrossRef]

45. *BS EN ISO 14855-1:2012*; Determination of the Ultimate Aerobic Biodegradability of Plastic Materials under Controlled Composting Conditions—Method by Analysis of Evolved Carbon Dioxide. ISO: Geneva, Switzerland, 2012.

46. Kijchavengkul, T.; Auras, R.; Rubino, M.; Ngouajio, M.; Fernandez, R.T. Development of an Automatic Laboratory-Scale Respirometric System to Measure Polymer Biodegradability. *Polym. Test.* **2006**, *25*, 1006–1016. [CrossRef]

47. Warren, F.J.; Gidley, M.J.; Flanagan, B.M. Infrared spectroscopy as a tool to characterise starch ordered structure—A joint FTIR–ATR, NMR, XRD and DSC Study. *Carbohydr. Polym.* **2016**, *139*, 35–42. [CrossRef]

48. Medina-Jaramillo, C.; Quintero-Pimiento, C.; Díaz-Díaz, D.; Goyanes, S.; López-Córdoba, A. Improvement of andean blueberries postharvest preservation using carvacrol/alginate-edible coatings. *Polymers* **2020**, *12*, 2352. [CrossRef]

49. Li, W.; Zheng, K.; Chen, H.; Feng, S.; Wang, W.; Qin, C. Influence of nano titanium dioxide and clove oil on chitosan–starch film characteristics. *Polymers* **2019**, *11*, 1418. [CrossRef]

50. Phothisarattana, D.; Wongphan, P.; Promhuad, K.; Promsorn, J.; Harnkarnsujarit, N. Biodegradable Poly (Butylene Adipate-Co-Terephthalate) and thermoplastic starch-blended TiO_2 nanocomposite blown films as functional active packaging of fresh fruit. *Polymers* **2021**, *13*, 4192. [CrossRef] [PubMed]

51. van Soest, J.J.G.; Vliegenthart, J.F.G. Crystallinity in starch plastics: Consequences for material properties. *Trends Biotechnol.* **1997**, *15*, 208–213. [CrossRef] [PubMed]

52. Morales, N.J.; Candal, R.; Famá, L.; Goyanes, S.; Rubiolo, G.H. Improving the physical properties of starch using a new kind of water dispersible nano-hybrid reinforcement. *Carbohydr. Polym.* **2015**, *127*, 291–299. [CrossRef] [PubMed]

53. Lai, D.S.; Osman, A.F.; Adnan, S.A.; Ibrahim, I.; Ahmad Salimi, M.N.; Alrashdi, A.A. Effective aging inhibition of the thermoplastic corn starch films through the use of green hybrid filler. *Polymers* **2022**, *14*, 2567. [CrossRef] [PubMed]

54. González-Seligra, P.; Goyanes, S.; Famá, L. Effect of the Incorporation of rich-amylopectin starch nano/micro particles on the physicochemical properties of starch-based nanocomposites developed by flat-die extrusion. *Starch-Stärke* **2022**, *74*, 2100080. [CrossRef]

55. Famá, L.; Rojas, A.M.; Goyanes, S.; Gerschenson, L. Mechanical properties of tapioca-starch edible films containing sorbates. *LWT-Food Sci. Technol.* **2005**, *38*, 631–639. [CrossRef]

56. Suh, J.H.; Ock, S.Y.; Park, G.D.; Lee, M.H.; Park, H.J. Effect of moisture content on the heat-sealing property of starch films from different botanical sources. *Polym. Test.* **2020**, *89*, 106612. [CrossRef]

57. Ochoa-Yepes, O.; Ceballos, R.L.; Famá, L. Effect of wheat and oat bran on the physicochemical properties of edible starch-based films obtained by extrusion for food packaging applications. *Starch-Stärke* **2022**, *75*, 2200087. [CrossRef]

58. Hajizadeh, H.; Peighambardoust, S.J.; Peighambardoust, S.H.; Peressini, D. Physical, mechanical, and antibacterial characteristics of bio-nanocomposite films loaded with Ag-modified SiO_2 and TiO_2 nanoparticles. *J. Food Sci.* **2020**, *85*, 1193–1202. [CrossRef]

59. de Menezes, F.L.G.; de Lima Leite, R.H.; dos Santos, F.K.G.; Aria, A.I.; Aroucha, E.M.M. TiO_2-enhanced chitosan/cassava starch biofilms for sustainable food packaging. *Colloids Surf. Physicochem. Eng. Asp.* **2021**, *630*, 127661. [CrossRef]

60. Chen, X.; Mao, S.S. Titanium dioxide nanomaterials: Synthesis, properties, modifications, and applications. *Chem. Rev.* **2007**, *107*, 2891–2959. [CrossRef] [PubMed]

61. Perotti, G.F.; Kijchavengkul, T.; Auras, R.A.; Constantino, V.R. Nanocomposites based on cassava starch and chitosan-modified clay: Physico-mechanical properties and biodegradability in simulated compost soil. *J. Braz. Chem. Soc.* **2017**, *28*, 649–658. [CrossRef]

62. Iovino, R.; Zullo, R.; Rao, M.; Cassar, L.; Gianfreda, L. Biodegradation of Poly (Lactic Acid)/Starch/Coir Biocomposites under Controlled Composting Conditions. *Polym. Degrad. Stab.* **2008**, *93*, 147–157. [CrossRef]

63. Briassoulis, D.; Mistriotis, A.; Mortier, N.; Tosin, M. A horizontal test method for biodegradation in soil of bio-based and conventional plastics and lubricants. *J. Clean. Prod.* **2020**, *242*, 118392. [CrossRef]

64. Castro-Aguirre, E.; Auras, R.; Selke, S.; Rubino, M.; Marsh, T. Insights on the aerobic biodegradation of polymers by analysis of evolved carbon dioxide in simulated composting conditions. *Polym. Degrad. Stab.* **2017**, *137*, 251–271. [CrossRef]

65. Luo, Y.; Lin, Z.; Guo, G. Biodegradation Assessment of Poly (Lactic Acid) Filled with functionalized titania nanoparticles (PLA/TiO_2) under compost conditions. *Nanoscale Res. Lett.* **2019**, *14*, 56. [CrossRef]

66. del Campo, A.; De Lucas-Gil, E.; Rubio-Marcos, F.; Arrieta, M.P.; Fernández-García, M.; Fernandez, J.F.; Muñoz-Bonilla, A. Accelerated disintegration of compostable ecovio polymer by using ZnO particles as filler. *Polym. Degrad. Stab.* **2021**, *185*, 109501. [CrossRef]

67. Lizundia, E.; Ruiz-Rubio, L.; Vilas, J.; Leon, L. Towards the development of eco-friendly disposable polymers: ZnO-Initiated thermal and hydrolytic degradation in poly (L-Lactide)/ZnO nanocomposites. *RSC Adv.* **2016**, *6*, 15660–15669. [CrossRef]

68. Qu, M.; Tu, H.; Amarante, M.; Song, Y.; Zhu, S.S. Zinc oxide nanoparticles catalyze rapid hydrolysis of poly (Lactic Acid) at low temperatures. *J. Appl. Polym. Sci.* **2014**, *131*, 40287. [CrossRef]

69. Tang, Z.; Chen, C.; Xie, J. Development of antimicrobial active films based on poly (Vinyl Alcohol) containing Nano-TiO_2 and its application in macrobrachium rosenbergii packaging. *J. Food Process. Preserv.* **2018**, *42*, e13702. [CrossRef]

70. Sethy, N.K.; Arif, Z.; Mishra, P.K.; Kumar, P. Nanocomposite film with green synthesized TiO_2 nanoparticles and hydrophobic polydimethylsiloxane polymer: Synthesis, characterization, and antibacterial test. *J. Polym. Eng.* **2020**, *40*, 211–220. [CrossRef]

71. Zamir, S.S.; Fathi, B.; Ajji, A.; Robert, M.; Elkoun, S. Biodegradation of Modified starch/poly lactic acid nanocomposite in soil. *Polym. Degrad. Stab.* **2022**, *199*, 109902. [CrossRef]

72. Cano, A.I.; Cháfer, M.; Chiralt, A.; González-Martínez, C. Biodegradation behavior of starch-PVA films as affected by the incorporation of different antimicrobials. *Polym. Degrad. Stab.* **2016**, *132*, 11–20. [CrossRef]

73. Suriyatem, R.; Auras, R.A.; Rachtanapun, P. Improvement of mechanical properties and thermal stability of biodegradable rice starch–based films blended with carboxymethyl chitosan. *Ind. Crops Prod.* **2018**, *122*, 37–48. [CrossRef]

74. Bher, A.; Unalan, I.U.; Auras, R.; Rubino, M.; Schvezov, C.E. Graphene modifies the biodegradation of Poly (Lactic Acid)-thermoplastic cassava starch reactive blend films. *Polym. Degrad. Stab.* **2019**, *164*, 187–197. [CrossRef]

75. *EN 13432*; Packaging—Requirements for Packaging Recoverable through Composting and Biodegradation—Test Scheme and Evaluation Criteria for the Final Acceptance of Packaging. ISO: Geneva, Switzerland, 2012.